Design, construction and verification of an Integral Field Spectrograph for the SCAR coronagraph

Author :	T.A. Stockmans
Student ID :	s1692488
Supervisor :	Sebastiaan Haffert. Msc.
	Emiel Por. Msc.
	Prof. dr. Christoph Keller
2nd corrector :	dr. Michiel de Dood

Leiden, The Netherlands, June 29, 2018

Design, construction and verification of an Integral Field Spectrograph for the SCAR coronagraph

T.A. Stockmans

Huygens-Kamerlingh Onnes Laboratory, Leiden University
P.O. Box 9500, 2300 RA Leiden, The Netherlands

June 29, 2018

Abstract

To make direct detection of planets like Proxima Centauri b possible, a high contrast coronagraph with a low inner-working angle is needed. With that in mind Por et al. designed the SCAR coronagraph. In SCAR the starlight is nulled using a SCAR phase plate and a single mode multicore fiber. In this thesis we describe the process of building a spectrograph for this instrument. After a small trade-off study, we have decided to build a prism spectrograph. Due to the proximity of the fibers, resolution increases in spite of bandwidth. The ultimate design has a resolution of 110 and a bandpass from 525 to 700 nm. The spectrograph was set-up and tested using a laser and a broadband source. The design induces a lot of crosstalk, therefore we used a special extraction method for the spectra described by Bolton and Schlegel. This technique creates a 2D model of the data and extracts accordingly. Finally we have been been able to retrieve spectra using this spectrograph and extraction method. This is a proof of concept for both the SCAR and the spectrograph behind it.

# Contents

1 | Introduction

1.1 Exoplanets

The search for exoplanets has witnessed a great rise since the discovery of the first exoplanet in 1995 [1]. Especially with indirect techniques, such as planet transits and radial velocity changes, thousands of planets have been found [2]. The biggest challenge in the field is now to directly image the planets. As can be seen in figure 1.1 our resolving power is sufficient for the planets around the stars close to us such as Proxima B when we use AO powered telescopes[3]. However, since most planets are a factor of 10^{-7} (or worse) fainter than their host star, it will be completely obscured by the Point Spread Function (PSF) of the star.

To make direct imaging possible, these AO powered telescopes have to be combined with coronagraphs of sufficient contrast (Difference between peak starlight before and after the coronograph). Aside from the contrast, the other important parameter for coronagraphs is the Inner-Working Angle (IWA), which is the minimal angular separation at which the contrast is achieved. The IWA is mostly given in $\frac{\lambda}{D}$. Most current coronagraphs cannot get a high enough contrast or otherwise have an inner-working angle (IWA) that is too big to directly image planets. Almost all optimization is fixed on enlarging, respectively reducing, these qualities.[4]

Another big challenge is combining the High Contrast Imagers (HCIs) as described above with a high-resolution spectrograph. Already we have happily made use of current spectroscopic data of planets: atmospheres have been crudely characterized and the first measurements of wind speeds have been made [5]. The acquisition of high-resolution data opens the window to a lot of useful and fruitful science[6].

1.2 Thesis outline

The process described in this thesis went as follows. First, there was a study to the possible spectrographs and a comparison following the specs needed for implementation with SCAR. After this trade-off study, we designed a low-resolution prism spectrometer. When the design was completed, we made measurements of the multicore SCAR in broadband- and

7
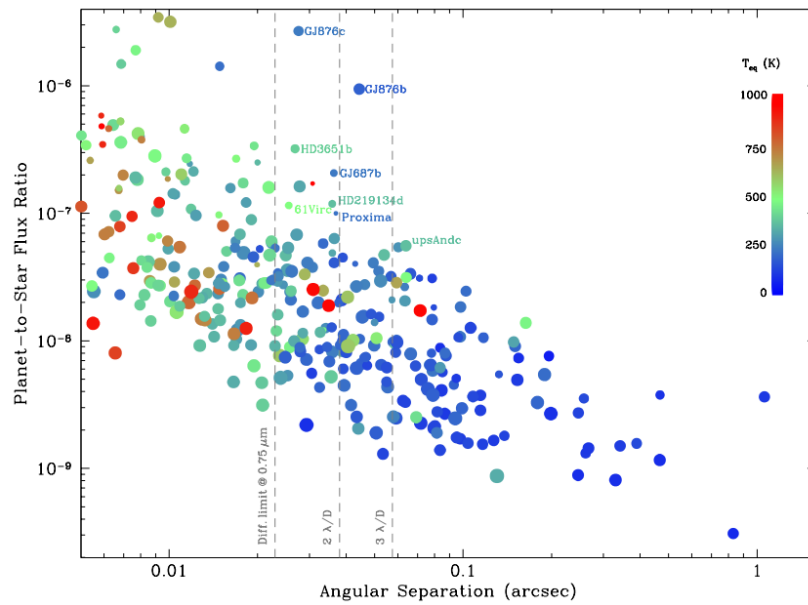
Figure 1.1: *The estimated contrast from known exoplanets is plotted against the angular separation between them and their primary star. The logarithm of the planet mass is depicted with the dot size, and the colorscale depicts their equilibrium temperature (adopting a common Bond albedo of 0.3). Vertical dashed lines show respectively the diffraction limit, 2 $\frac{\lambda}{D}$ and 3 $\frac{\lambda}{D}$ thresholds for the 8.2-m VLT at 750 nm (corresponding to the O_2 A-band). Retrieved from [3]*

laserlight and measured the quality and propagation of the dispersion. SCAR has previously been tested and characterized with laserlight with a single-core, single-mode fiber [7], but its broadband reaction is yet unexplored, as well as everything surrounding the multi-core fiber. After several years -and thus beyond the scope of this thesis- the goal is to directly observe a planet with an instrument based on the techniques first explored by this instrument (or this instrument itself).

The underlying technology is explained in chapter 2 starting from coronagraphs to optical fibers to ultimately SCAR itself. In chapter 3 the design is showed, as well as the models that confirm it. At the end of chapter 3 is an explanation of the algorithm that will be used to analyze the data from the spectrograph. The raw results and processed data are shown in chapter 4, eventually ending in chapter 5 with the implications and some remarks on the instrument.

2 | Theoretical Outline

2.1 Coronagraphy
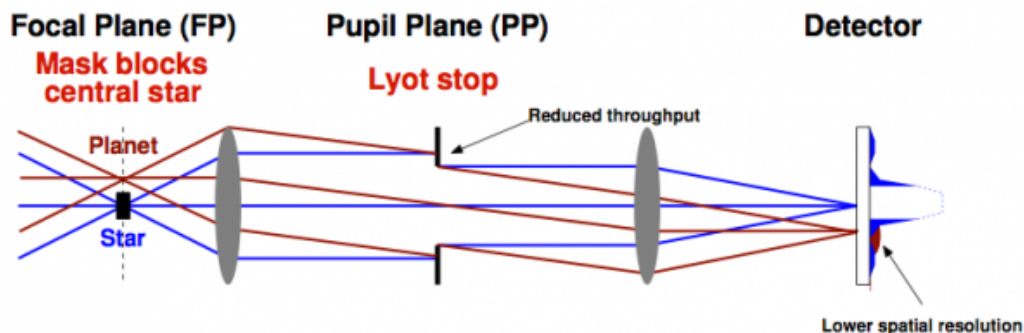
Figure 2.1: *A Sketch of the working of the Lyot coronagraph. Retrieved from [8]*

A coronagraph is an instrument which suppresses starlight, while ideally not affecting everything surrounding the star. Important quantities are contrast and the inner-working angle. The former depicts the difference between the original peak star flux before and after the coronagraph. The latter depicts the minimal angular separation where this contrast is achieved.

The first coronagraph was made in 1939 which consisted of a mask in the focal plane obscuring the star and an aperture in the pupil plane (a so-called Lyot-stop) obscuring residuals. This is still one of the most used coronagraphic techniques because of its simplicity, although different techniques with better nulling and smaller IWA are gaining in popularity [4].

One of these new techniques to null starlight is by making use of interference of light. By applying a π phase-difference between two light-waves, they will destructively interfere. This has opened up a new way of coronagraphy, suppressing starlight far more efficiently than the classical Lyot coronagraph [9]. All coronagraphs described below follow this principle.
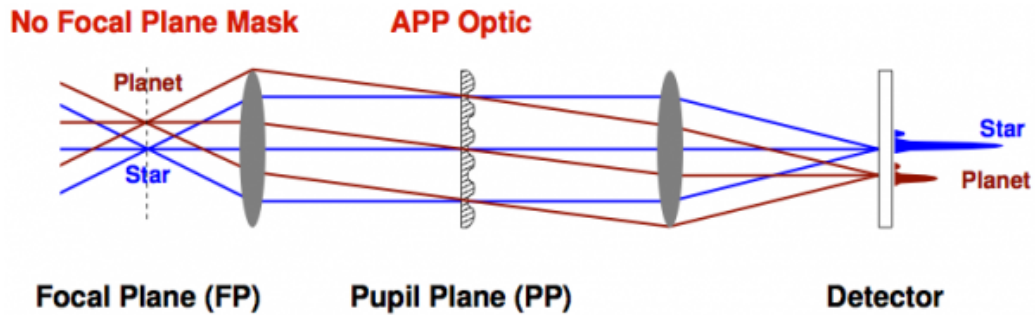
11

No Focal Plane Mask   **APP Optic**

Planet

Star

Focal Plane (FP)   **Pupil Plane (PP)**   **Detector**

Star

Planet

Figure 2.2: *A Sketch of the working of the APP coronagraph. Retrieved from [8]*

2.1.1   Apodizing Phase Plate (APP)

This coronagraphic technique is the main predecessor of the vector Apodizing Phase Plate (vAPP) that is described below. An APP consists of a Phase Plate in the pupil plane that modifies incoming PSFs in such a way that starlight is nulled, possibly rendering a planet visible. The Phase Plate is a glass of high refractive index with a varying thickness. Because of this varying thickness, a phase difference is induced in the light which will interfere destructively. This phase difference ($\Delta\phi$) is described in equation 2.1, where Δx is the difference in thickness of the material, n the refractive index and λ the wavelength of the light.

$$\Delta\phi = 2\pi\frac{\Delta\lambda}{\lambda} = 2\pi(n_{plate} - n_{surrounding})\frac{\Delta x}{\lambda} \tag{2.1}$$

The phase plate is located in the pupil plane instead of the focal plane, which causes all incoming PSFs to be affected exactly the same, without making a distinction between host star, companion or background star. The plate is designed by selecting a region of the PSF and calculating the necessary phase pattern that will null this region out. The choice of the region affects the quality of the null. Bigger regions will be nulled less effectively, while small regions will have a very effective null. Almost all shapes can be made this way, although the D-shaped pattern with approximately half of the PSF obscured is most common since the size of the region versus the quality of the null is optimized [10] [11] [12].

A great advantage of this method is its low sensitivity to tip-tilt errors or perfect alignment of the star and the center of the coronagraph (since the whole image is modified and not only the center of the coronagraph). Moreover, it only consists of one optic which simplifies implementation

and alignment significantly [10]. However, one huge disadvantage of this method is the important dependence on the wavelength for the phase difference and thus indirectly the nulling.

2.1.2   vector Apodizing Phase Plate (vAPP)

The vAPP is based on a similar principle as the APP. Only, instead of changing the classical phase by differentiating the distance travelled through a medium, it makes use of the geometrical phase difference. Geometrical phase is the phase of circularly polarized light. Starlight is unpolarized and can thus be split equally in two circularly polarized components with opposite handedness.

The vAPP makes use of optics called retarders which consist of a crystal with a refractive index dependent on the polarization of the light. These materials have a fast-axis, which is the axis of polarization where the refractive index is at its minimum. This is perpendicular to the slow-axis which is where the refractive index is at its maximum. This way, a $\frac{\lambda}{2}$-plate can be made, where the delay between fast-axis light and slow-axis light is exactly half of a wavelength. When light with a linear polarisation rotated an angle θ from the fast-axis passes through, it will be rotated even further to an angle of 2θ. Circular polarisation will flip its handedness and it will pick up a phase difference with the light with an opposite handedness governed by equation 2.2.

$$\Delta\phi = \pm 2\theta \tag{2.2}$$

The phase difference is now induced by the angle to the fast-axis instead of the width of the optic. Since we can achromate the $\frac{\lambda}{2}$ plates with techniques described in [13], this technique does not have the achromaticity of the APP [11] [12]. As with the APP, the electric field can be modified in almost every shape.

2.1.3   Optical fibers

Optical fibers have seen multiple uses in astronomy. Especially in combination with spectrography, there have been multiple instruments designed which made use of optical fibers [14]. The working of an optical fiber, also known as waveguides, depends on total internal reflection on an inner surface made from silica. When incident light is confronted with a medium
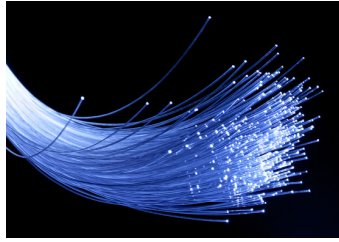
(a) *Picture of a bundle of backward illuminated fibers. Retrieved from [16]*
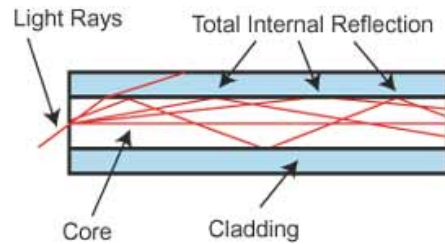
(b) *Schematic image of a fiber. The cladding is glass with a higher refraction index than the glass of the core. Retrieved from [17]*

with a different refractive index, the light will be partially reflected and partially refracted. This refraction is governed by Snell's law and from this follows the existance of an angle of incidence where the refracted angle is more than 90 degrees from the outward normal, known as the total reflection angle [15].

All the light that is not absorbed by the outer cladding, will therefore be reflected inside the fibercore, guiding the light through the fiber. The fiber can even be bent and deformed (until breakage occurs, without heavily affecting the output, because of its reliance on reflection. This means that information can easily be transferred from one place to another without significant losses. Shining the light with the right angle and correct properties in the fiber is called coupling or injection [15].

There are two main kinds of Optical Fibers: Multi mode (MMF) and single mode (SMF). In a MMF almost all modes of light can be coupled efficiently, provided that it has the right angle of incidence and wavelength range. With SMF only one mode can be coupled efficiently (The Gaussian mode). A mode is the radial profile a lightwave has from the center of the spot outwards. These modes are mostly described with Hermite-Gaussian modes, the simplest (zeroth order) is a profile following a 2D Gaussian distribution around the center of the beam [15]. The intensity of a Gaussian beam in our calculations is described by 2.3 [18], where r is the radial distance from the center of the beam and ω is the so-called spotsize

$$I(r) = I_0 \cdot e^{\frac{-2 \cdot r^2}{\omega^2}} \tag{2.3}$$

An important variable used for fibers is the Mode field diameter (MFD).

This is the diameter of the beam where the intensity has fallen off to $\frac{1}{e^2}$ of its maximum. In a Gaussian beam with an intensity profile governed by equation 2.3, this is equal to 2ω. The MFD is a factor $\sqrt{\frac{2}{\ln 2}}$ larger than the FWHM (point where the intensity is half of its maximum).

The optical fiber is created by warming up a glass block with the required holes and slowly stretching it to a length of around 100 meter under a temperature of 2000 degrees Celsius [19].

2.1.4   SCAR

The SCAR coronagraph (Single mode Complex Amplitude Refinement) is designed by Por et al. in 2017. It is based on a combination of a single mode fiber array, a microlens array and a pupil-plane SCAR Phase plate (PP). Incoming light is first modified by the PP as described in subsection 2.1.2 with one big difference described below. After this Phase Plate, it will be focused using a lens on a microlens array. This microlens-array focusses the light even further for it to couple in the fibercores, see figure 2.4.

In a regular vAPP coronagraph the intensity of the starlight on the location of the planet will be suppressed by the PP using destructive interference. The SCAR phase plate, however, will not reduce the intensity directly, it will only modify the electric field. Only after the single mode fiber the nulling is visible. This is because the electric field inside a single mode fiber is the weighted average of the coupled electric fields (with the weight determined by the radial distance from the center). Therefore, when the electric field is on average zero when coupled with the fiber, there will be no outgoing intensity.

Finally, a higher contrast than with a single vAPP can be achieved by making use of this single mode property in two ways. First, the PP does not have to correct higher order modes, enabling a better nulling in the Gaussian mode and reducing leakage of starlight to the image. Second, the PP only has to average the electric field in the regions, instead of directly reducing the intensity which is less efficient.

The destructive coupling (coupling of an electric field that is zero on average) can be done with a so-called first-order null or a second-order
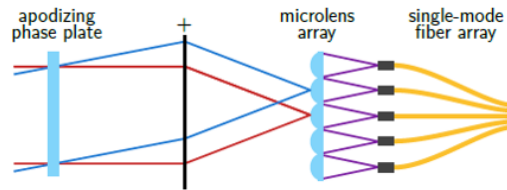
Figure 2.4: *A schematic drawing of the SCAR coronagraph. The incoming light is first modified using a PP and then focussed by a lens on the microlenses. These microlenses focus the light in the fibercores. Retrieved from [20]*

null. The important property of the PSF here is that the first Airy ring has a π phase difference with both the Airy core and the second ring. The first-order null consists of only interfering the first Airy ring with the second ring. This method is extremely prone to be reduced in efficiency by tip-tilt errors, since less coupling of the second ring means less destructive interference and more leakage of starlight into the image.

The second-order null is created differently. Instead of using only the second ring for interference with the first, both the core and the second ring are used. Most of the Airy core of the PSF should be focussed on the center fibercore, but a fraction on the directly surrounding fibercores together with the first Airy ring and a fraction of the second Airy ring. This second order null is far less subject to small tip-tilt errors, since these errors only shift the percentage of Airy-core versus Second Airy ring. This percentage-shift would not influence the total null significantly.

The important function of the microlenses in this design is the correct coupling of the PSF parts with the fibercores. To couple the second Airy ring as well as part of the Airy core into the same fibercore would otherwise be too much prone to aberrations and vibrations. It is impossible to get the same coupling factors with external focussing.

This configuration creates a high-contrast ($2 - 3 \cdot 10^4$) around the star with an IWA of approximately $1\frac{\lambda}{D}$, theoretically making the detection of planets like Proxima b possible (as seen in figure 1.1) [7] [20]

2.2 Spectrographs

In this section different kinds of spectrographs and their use for implementation in the SCAR instrument is displayed. The first prerequisite is that
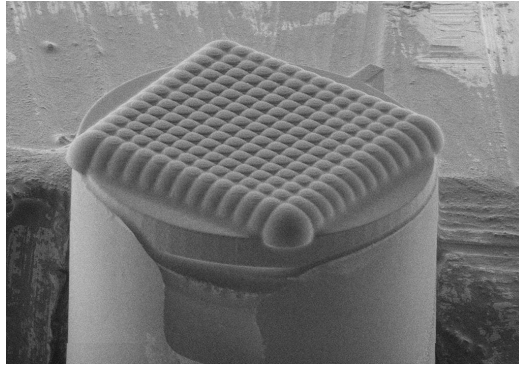
Figure 2.5: *Microlenses on the tip of the SMF. Imaged with a SEM with a 400 times magnification. Notice that there are 13x13 microlenses, this is purely to get rid of edge effects. The outer lenses focus right in the cladding, while the inner fibers all focus in a fibercore.*

the throughput has to be as high as possible, since a planet should still be detectable and not lost in the noise. The second requirement is that a sufficient bandwidth is covered by the spectrograph (~200 nm) for upcoming research. Third, the resolution (which is the ratio of used wavelength over the distinguishable wavelength fraction $\frac{\lambda}{d\lambda}$) does not necessarily have to be high, everything above 60 would be enough.

Finally, we desire the capability to retrieve the spectrum from an image quick enough. This is needed because eventually we would like to be able to measure speckles in the system which are time dependent and variable on a short timescale. Speckles are deformations of the wavefront of the light due to the atmosphere or aberrations in the alignment. The so-called Atmospheric coherence time is a good parameter to quantify the variation timescale of the first kind of speckles. The Atmospheric coherence time is given by equation 2.4 with r_0 the Fried parameter and V_0 the average wind speed.

$$\tau_0 = 0.314 \frac{r_0}{V_0} \tag{2.4}$$

This coherence time was calculated for the Roque de los Muchachos on the Canary Islands(a prime location of telescopes)to be on average 4.9 ms [21]. The retrieval of the spectrum thus has to be done within half of this time for it to be able to always give correct results.

2.2.1 Prism

A prism spectrograph is the oldest known spectrograph. It makes use of the wavelength dependent refraction of glass (or other transparent material) to disperse the light. This dispersion occurs twice (on two sides of the prism) and returns a spectrum at the end. Prisms have a high throughput of approximately 95% making them ideal for low-resolution spectrographs. The dispersion is generally not enough for high resolution with most common CCD's, but a resolution of ~100 is easily achieved. [22]

2.2.2 Gratings

Due to its wavelike nature, light will spread out when it hits a slit. When there are multiple slits next to each other, the outcoming light of these slits will interfere constructively according to $m\lambda \simeq d \sin\theta$ and destructively according to $(m + \frac{1}{2})\lambda \simeq d \sin\theta$. Here is m an integer called the "order" and θ the angle of incidence onto the slits. This interference is wavelength dependent and makes it a spectrograph. The light will be dispersed over multiple orders which lowers the throughput significantly compared to prism spectrographs. The resolution is determined by the order of the inspected diffraction (the m) and the number of slits in the grating. [22]

The same principle also holds with, instead of slits, a grooved reflective surface (a "blazed" grating or echelette). By making use of an echelette, the number of order can be as high as ~100, enabling a resolution such as 115000 [22] [23].

2.2.3 Fabry-Perrot

A Fabry-Perrot spectrograph makes use of the workings of a cavity. A cavity is made of two mirrors facing each other. If the distance of the mirror is a multitude of the wavelength, it will interfere constructively inside the cavity and ultimately get a throughput of ~99%. All the other wavelengths will interfere destructively and thus won't pass through. This creates an extremely high resolution, but with a very narrow bandwidth. It would be possible to change the distance of the two mirrors and scan different wavelengths, but this requires making multiple images very fast while accurately controlling the distances.

To get the minimum resolution of 60, we would have to make 60 images in 2.45 ms which comes down to one image every 0.04 ms. This means not enough integration time to clearly see something. [22]

2.2.4 Fourier transform

The Fourier Transform spectrograph is an adaptation of the Michelson interferometer. The incoming beam is split by an ideal (50/50) beam-splitter and reflected back by two mirrors. These reflections combine again at the same beam-splitter and will transmit or reflect again. The beams will interfere constructively or destructive depending on the relative path lengths the light has to travel and the wavelength of the light. If a wavelength is visible or not depends therefore on the separation of the arms. By changing this with a certain frequency, we can Fourier transform the resulting datacube and retrieve the spectrum.

Most Fourier transform spectrographs have a high resolution, but they all demand scanning in time to be able to transform it back to spectra. The timeframe due to the atmosphere is too narrow to get correct and precise measurements with this kind of spectrograph. [22]

3 | Methods

3.1 Theoretical Setup

After the small trade-off study of above, we have decided to build a prism spectrograph. This is based on the prerequisite of the applications that the retrieval of the spectra has to be fast enough, which limits the possibilities to a prism or a grating. Furthermore, since the throughput of the prism is about 95% and the throughput of the grating is significantly less, we have decided on a prism spectrograph. Below is a step for step explanation and specification of the design displayed. To get an instant overview of the set-up, please refer to figure 3.2. A full overview of the used components can be find in table 3.1.

The fiber is made in Bath, England and its properties are described in [24]. It has a MFD of $\sim 1.84\mu m$, an outgoing numerical aperture of 0.22 and an average spacing between the cores of $10.53\mu m$. The fiber is sent to the Karlsruhe institute of Technology in Germany where they use direct write two-photon lithography (inducing a chemical reaction with a highly localised laser-focus to remove material)[25] to print the microlenslets on one end of the fiber. It has already been shown that with this technique these lenslets can achieve an effective coupling of up to 88% of incident laserlight with the fibercores [26].

The design of the spectrograph starts with a microscope-objective (f = 20mm) that collimates the fiber-outcome, this was chosen since it has a numerical aperture of 0.28 and will thus be able to collimate the beam that comes out of the fiber without much aberrations. The collimated beam will be refocussed by a lens of 150 mm focal length resulting in a 7.5 times magnified focus, which enables the possibility of obscuring a single row of fibercores by a wire of 100 μm. In this way, we can obscure the fibercore containing the star, enabling longer exposure times without saturating the CCD. After the refocus a 150 mm lens will collimate the beam again for it to pass through the prism in the pupil plane.

The prism has an apex angle of 18 degrees (corresponding with its angle of incidence) and is made from BK7 glass. BK7 has a refractive index of 1.5163 and a refractive index change of $\frac{dn}{d\lambda} = 0.03947\mu m^{-1}$ at the configuration wavelength of 600 nm [27]. Using equation 3.1, the resolution can be calculated.

21

$$R = \frac{\lambda}{d\lambda} \tag{3.1}$$

This can be rewritten using the diffraction limit $d\theta = \frac{\lambda}{D}$ and two more components. The first being the differential of the angle to the refractive index and the second being the differential of the refractive index to the wavelength:

$$
\begin{aligned}
R &= \lambda \cdot \frac{d\theta}{d\lambda} \cdot \frac{1}{d\theta} \\
  &= \lambda \cdot \frac{d\theta}{dn} \cdot \frac{dn}{d\lambda} \cdot \frac{1}{d\theta} \\
  &= D \cdot \frac{d\theta}{dn} \cdot \frac{dn}{d\lambda}
\end{aligned}
$$

The diameter of the beam can be calculated by making use of the outgoing numerical aperture of the fiber and the magnification of the lenses.

$$D = 2 \cdot NA \cdot f_1 \cdot \frac{f_3}{f_2} \tag{3.2}$$

To calculate $\frac{d\theta}{dn}$, one starts off with the equation for the angle deviation by the prism, graphically shown in figure 3.1. Here, e is the outgoing angle of the beam with respect to the prism, n is the refractive index, i is the angle of incidence and α the apex angle of the prism.

$$e = \arcsin(n \cdot \sin(\alpha - \arcsin(\frac{\sin i}{n}))) \tag{3.3}$$

By differentiating this equation with respect to the refractive index of the prism, equation 3.4 is derived.

$$\frac{d\theta}{dn} = \frac{\sin(i) \cdot \cos(\alpha - \frac{n}{\sin(i)})}{\sqrt{(1 - \frac{\sin^2(i)}{n^2}) \cdot n}} + \frac{\sin(\alpha - \arcsin(\frac{\sin(i)}{n})))}{\sqrt{1 - n^2 \cdot \sin^2(\alpha - \arcsin(\frac{\sin(i)}{n}))}} \tag{3.4}$$

The rewriting was necessary to be able to make use of readily available properties of the prism and light in determining the resolution.

After being dispersed by the prism, all the light will be focussed using a 500 mm lens resulting in an additional magnification of $3\frac{1}{3}$ on the CCD.
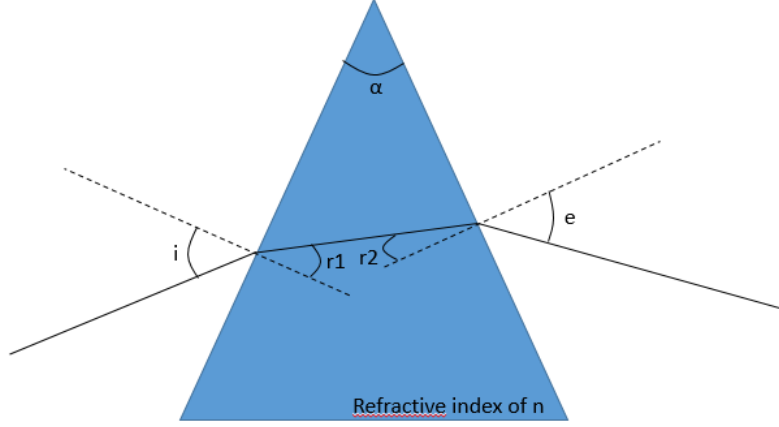
Figure 3.1: *A beam coming in from the left of the prism with angle to normal i is refracted due to Snell's law to exit with an angle to normal e. The apex angle is α and the refractive index of the material is n.*

The total magnification is a factor 25, enlarging the MFD to $46\mu m$. Since the pixelsize of the CCD is $16\mu m$, the Nyquist criterium is abided.

Using the focal length of the last lens and the total magnification of the system, the bandwidth ($\Delta\lambda$) can be calculated using the following equation:

$$\Delta\lambda = \frac{\Delta\theta}{\frac{d\theta}{dn} \cdot \frac{dn}{d\lambda}} \tag{3.5}$$

Where $\Delta\theta$ is the maximal angular separation of the fibers. This maximal spatial separation is calculated as follows:

$$\Delta x = \frac{d \cdot M}{\sin(\tilde{\zeta})} \tag{3.6}$$

with $\tilde{\zeta}$ the best rotation angle of the fibers, M the magnification and d the distance between adjacent fibercores in the fiber. To convert this to an angular separation, the focal length of the last lens should be used:

$$\Delta\theta = \arctan(\frac{\Delta x}{f}) \tag{3.7}$$

After plugging in all parameters of the used prism and lenses, we expect a resolution of ~110 and a bandwidth of 200 nm. Two filters in the

Table 3.1: *A table showing the specifics of all components, useful for reproduction*

| Designation	Seller	Component	Spec	Part number
L1	Edmund Optics	Mitutoyo Plan APO Infinitely corrected Long WD Objective	f = 20mm	#46-144
L2/L3	ThorLabs	Unmounted Positive Achromatic Doublets	f=150mm	AC254-150-A
L4	ThorLabs	Unmounted Positive Achromatic Doublets	f = 500mm	AC254-500-A
Prism	ThorLabs	Round Wedge Prism	AR coating 350-700 nm	PS814-A
F1	Edmund Optics	High Performance OD4 Longpass Filter	525 nm cut-off 25 mm Diameter	#84-744
F2	Edmund Optics	High Performance OD4 Shortpass Filter	700 nm cut-off 25 mm Diameter	#84-714
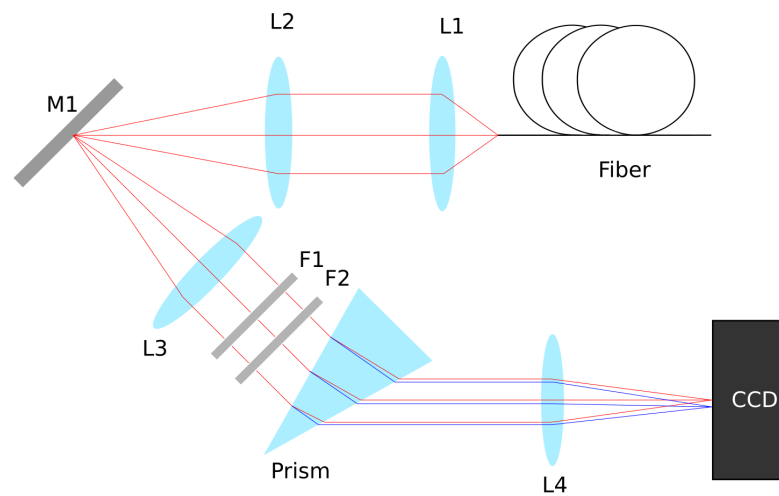
Figure 3.2: *A schematic representation of the design. L1 to L4 are the lenses, M1 is a mirror and F1 and F2 are the filters. The image is not to scale*

collimated beam between lens 2 and the prism should make sure that no overlap between spectra occurs when the dispersion happens under the correct angle. These filters create a bandpass between 700 nm and 525 nm (see figure 3.4). The total set-up is 1.64 meters long and consequently has to be folded with extra mirrors to fit on the table.

3.1.1   Models

We ran this set-up through Zemax and got a sufficient separation and resolution for the calculated bandwidth as can be seen in figure 3.5. All used wavelengths should render a clear image and the dispersed light from one fiber shouldn't overlap with the one next to it.
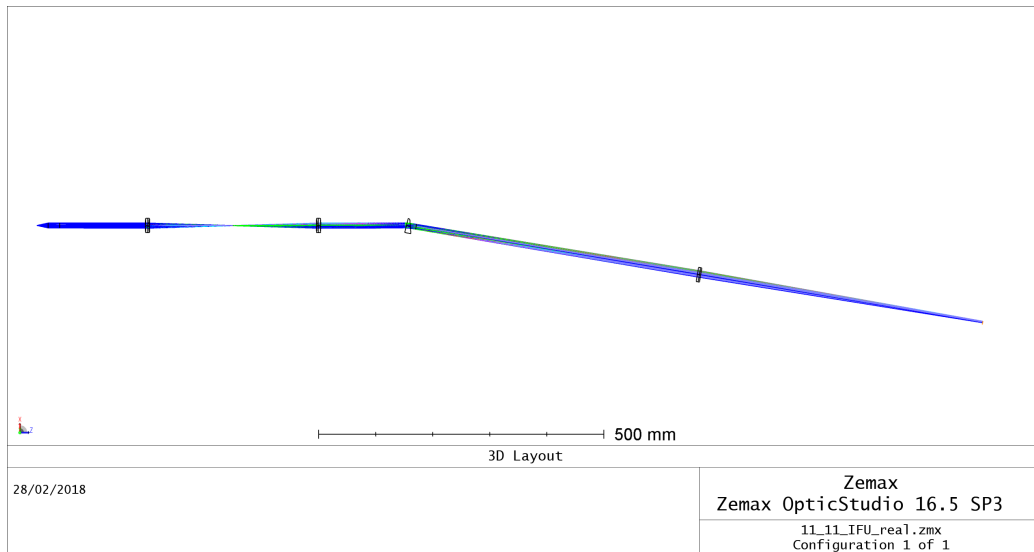
Figure 3.3: *The design as envisioned in Zemax. It reads off from left to right with Fiber, Lens 1, Lens 2, Slit, Lens 3, Prism, Lens 4, CCD.*
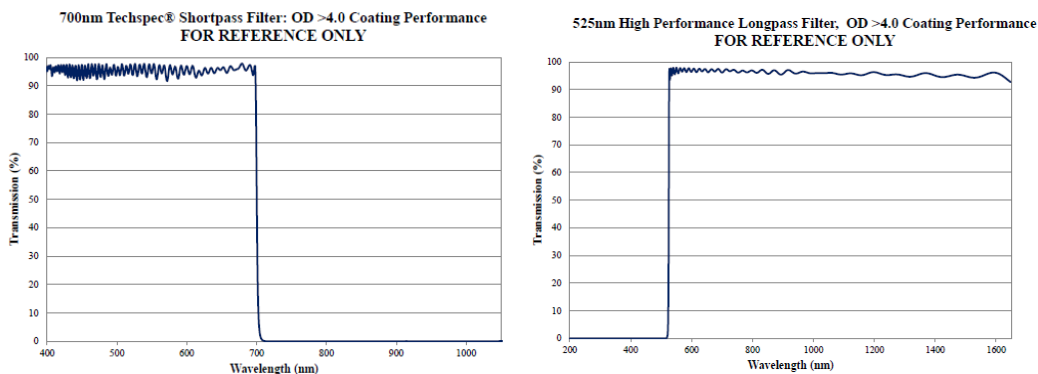
(a) *Shortpass filter of 700 nm*


(b) *Longpass filter of 525 nm*

Figure 3.4: *The transmission plots of the used filters. On the x-axis is the wavelength and on the y-axis the transmission. Retrieved from [28] and [29].*

3.1.2   Rotation

If the dispersion would be directly to the right, the bandwidth that can be achieved would be far from optimal. To optimize the bandwidth, the fibers would have to be dispersed under an angle. This angle has been calculated using a python simulation. In this simulation, the fibercores are dispersed until they overlap with another fiber. An overlap is a separation of less than one MFD between two fibercores. From this simulation, the

Figure 3.5: *The design modelled in Zemax. On top are the outer spots of two fibercores next to each other with the airy ring (black ring) on respective the left/right fiber outer spot. These spots lay more than $\frac{\lambda}{D}$ apart, making them distinguishable. The spotsize is dependent on the wavelength, causing the 500 nm to be much larger than the 675 nm spot. Down left is the spotdiagram of 11 fibercores, notice that they all fall in the airy radius indicating a diffraction limited image. Downright is the wavefront error due to the optics plotted against the wavelength, where the displayed black line depicts the diffraction limit. Since the wavefront-error is under the diffraction limit for all wavelengths, this will not affect the image.*
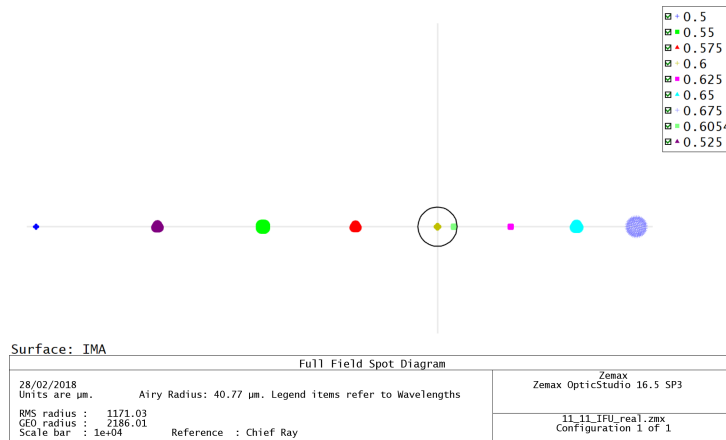
Figure 3.6: *This figure shows a validation of the resolution we calculated. The dots differ in color by the calculated $d\lambda$ which spatially separates them by $\frac{\lambda}{D}$ (black circle)*

optimal rotation is calculated to be 9.86 degrees and displayed in figure 3.7.

3.2 Planned Measurements

To test the complete working of the system, first the fiber and all elements of the spectrograph have to be aligned using a laser uniformly illuminating all fibercores. After alignment, an image using this uniform laser input can be made. From this image the brightness of all individual fibercores can be measured, as well as the FWHM and the average core separation.

The next step is uniformly illuminating all fibercores using a broadband source. This will prove if it is possible to extract a spectrum for each fibercore and whether the design performs as expected. Two important properties are the overlap of the spectra and the crosstalk. The crosstalk is how much signal of one core will interfere with the one directly adjacent to it. When the crosstalk is high, the individual spectra are harder to distinguish and it cannot be determined whether light in between the spectra belongs to one or another. If the crosstalk is too high, an individual spectrum cannot be extracted.

After we have the spectra from the broadband source, a line lamp or multiple lasers can be used to find the wavelength solution. This solution is necessary since there is no linear relation between wavelength and
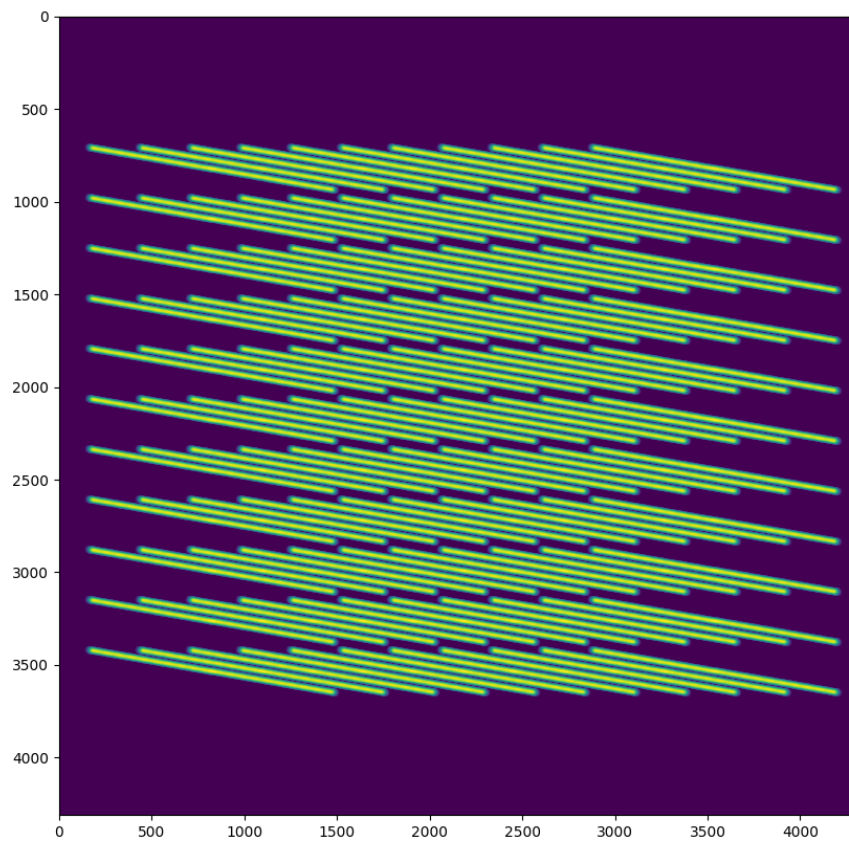
Figure 3.7: *The simulated light from 121 fibercores after having been dispersed at a 9.86 degree angle until overlap with the next fiber.*

dispersion. This non-linearity is caused by a higher order wavelength dependence in the refractive index of the prism and in $\frac{d\theta}{dn}$.

After these measurements, the next step is to integrate the system with the SCAR Phase Plate and an adaptive optics system and measure the difference in throughput and the quality of the nulling due to the fiber.

3.3   Spectrum extraction

Going from the CCD image towards a spectrum for each individual core requires a special extraction method. From each fibercore a 2D Gaussian is expected to come out when the source behind it is a laser. Each wavelength will have this pattern of 121 2D Gaussians, only spatially shifted since the angle of refraction is different in the prism. When a broadband source is used all the Gaussian patterns will overlap, resulting in a continuous bar of light.

3.3.1   Basic reduction of raw data

The usual reduction starts off by removing a dark (K) from the raw data (C). A dark is an image taken with the shutter closed and the same exposuretime as the original image, to reduce noise multiple darks are averaged to one ultimate dark. After this, the camera's sensitivity is divided out by use of a flat (F). This flat is an image of the same exposure time of an uniform light source of the CCD (such as twilight or the inside of the dome shone upon with an incandescent lamp). From the flat we also first subtract the dark and stack multiple flats into one. The last step is removing the Sky (S), which is a weighted average of the reduced image with an exclusion from the source and clear flaws. In this way the reduced image (R) is retrieved. [30]

$$D = \frac{C - K}{F} \tag{3.8}$$

$$S = FIT(D) \tag{3.9}$$

$$R = D - S \tag{3.10}$$

$$\tag{3.11}$$

3.3.2   Basic Extraction

The classical method of extracting a spectrograph is expertly described in [30]. The most simple extraction method consists of first reducing the data as described above, neglecting all pixels seemingly hit by cosmic rays or malfunctioning significantly. After reduction, all pixels concerning one spectrum are added in the direction perpendicular to the dispersion direction (so-called spatial direction).

An optimization of this method also corrects for the noisy pixels, cosmic ray hits or sudden malfunctioning. This method reduces the statistical error while preserving the photometric accuracy. This is done by assigning a weight to all pixels determined by its variance and mean value. Thus pixels which are faint but rapidly varying will be given less weight than bright constant pixels. Furthermore, cosmic ray hits are detected by looking at how much the spatial profile (profile perpendicular to the spectral profile) deviates from a model of the spatial profile. By giving a new weight to all pixels, a new variance will be detected for all pixels. To get rid of introduced biases, this working method has to be iterated until it converges for each pixel [30].

However, these methods have one big disadvantage for the spectra from the SCAR-spectrograph. The spectrograph is designed to have as much bandwidth as possible for its resolution. This means that the crosstalk between the spectra is extremely significant. In the aforementioned paper, spatial profiles of five pixels is mentioned in one of the examples, but in the SCAR-spectra already half of the pixelcounts are due to the adjacent spectrum at this spatial distance. The spectrograph is simply too aggressively designed for the methods of above to be feasible. That is why there will be made use of a different spectral extraction method.

3.3.3   Position determination

The most important step to retrieve a spectrum that can be trusted is a correct determination of all the locations of all the fibercores. All the measurable cores are found by looking at where there is a steep reduction in light on the right side, since this indicates cut-off by the filters.

These starting points are refined by looking at the brightest pixel in its neighbourhood. Starting from this starting position two methods are

(a) Simulated spectrum   *(b) Working of the Algorithms on the slice*
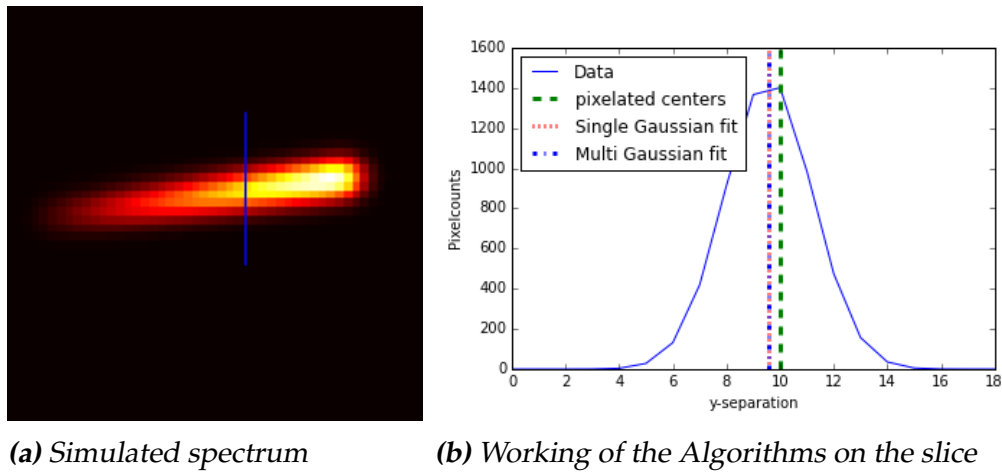
Figure 3.8: *A simulation of one spectrum with its centrum found with PeakUtils and the Least-squares fit. The left plot is a cut-out along the line in the right image*

used to retrieve the tracks of the spectra. First, using the python package PeakUtils, an 1D Gaussian is fitted vertically over the spectrum. PeakUtils gives a pixel value of the centers of the fitted Gaussians and a subpixel determination of the centers using interpolation. The second method is a linear least squares fit of multiple Gaussians with the pixel-values of PeakUtils as a first estimate. This is repeated sideways over the whole spectrum, mapping all the spectra on a subpixel-level. See figure 3.8 for a simulation of these methods.

3.3.4   Linear Algebraic Extraction

Instead of the basic method of above, a linear algebraic extraction will be used. This method is described in [31]. The spectrum of a single fibercore in the detector plane can be expressed as a sum over all wavelengths of the corresponding Gaussian PSFs. This summation is a linear operation which means that a matrix can be constructed that transforms an amplitude profile directly into an detector-image (unraveled to a 1-D vector) see equation 3.12.

$$\mathbf{p} = \mathbf{M}\mathbf{f} + \mathbf{n} \qquad (3.12)$$

Here $\mathbf{p}$ is the 1D unraveled version of the original image, $\mathbf{f}$ is the amplitude profile (the spectrum itself) and $\mathbf{n}$ is the noise vector, which is assumed to be zero. $\mathbf{M}$ is a matrix containing all the Gaussians for all

fibercores that we would like to retrieve. For one fibercore all the corresponding wavelengths should have the same amplitude to get an unbiased spectrum. Ideally, the FWHM of the Gaussian should increase with wavelength to come closer to reality, but this is beyond the scope of this thesis and can only be done when one has the wavelength solution.

To create $\mathbf{M}$ an image is created containing only the Gaussian of one fibercore and one wavelength, this 2D-array is reshaped to a 1D vector by adding all the columns after one another. The next wavelength is treated in a similar way and added after the previous one etc., creating a 2D array for one fibercore. The next fibercore is dissected the same and afterwards all cores will be put under each other in a huge, largely sparse, 2D array. See figure 3.9 for a visualization.

This array has to be inverted, which is computationally the hardest part. The matrix is *mxn* matrix, thus inversion can only be done with a so-called pseudo-inverse[32]. To do this, a single value decomposition algorithm is used (scipy.sparse.linalg.svds). This algorithm factorizes the matrix in the following way:

$$\mathbf{M} = \mathbf{U}\mathbf{\Sigma}\mathbf{V}^* \tag{3.13}$$

Here $\mathbf{U}$ is a unitary *mxm* matrix (its inverse is the same as its conjugate transpose [32]) containing all left singular vectors (eigenvectors of $\mathbf{M}\mathbf{M}^*$) as columns. $\mathbf{V}^*$ is the conjugate transpose of $\mathbf{V}$, which is a unitary *nxn* matrix containing all the right singular vectors (eigenvectors of $\mathbf{M}^*\mathbf{M}$). $\mathbf{\Sigma}$ is a diagonal *mxn* matrix containing square roots of all non-zero eigenvalues of $\mathbf{M}^*\mathbf{M}$ or $\mathbf{M}\mathbf{M}^*$.

To get the pseudoinverse (Moore-Penrose inverse):

$$\mathbf{M}^+ = \mathbf{V}\mathbf{\Sigma}^+\mathbf{U}^* \tag{3.14}$$

where $\mathbf{\Sigma}^+$ is ideally created by replacing every diagonal non-zero element of $\mathbf{\Sigma}$ by one over this element and then conjugate transposing. However, since we expect to find mostly noise in the wings of the Gaussians, a quadratic regularisation is introduced. Instead of using the simple multiplacated inverse of each element in $\mathbf{\Sigma}^+$ each element σ_i is replaced by:

$$\sigma_i \rightarrow \frac{\sigma_i}{\sigma_i^2 + \alpha^2} \tag{3.15}$$

with $\alpha = \mathbf{max}(\sigma) * r_{cond}$ the regularisation factor. This factor makes sure that all low values of σ are slowly flattened out, reducing their im-
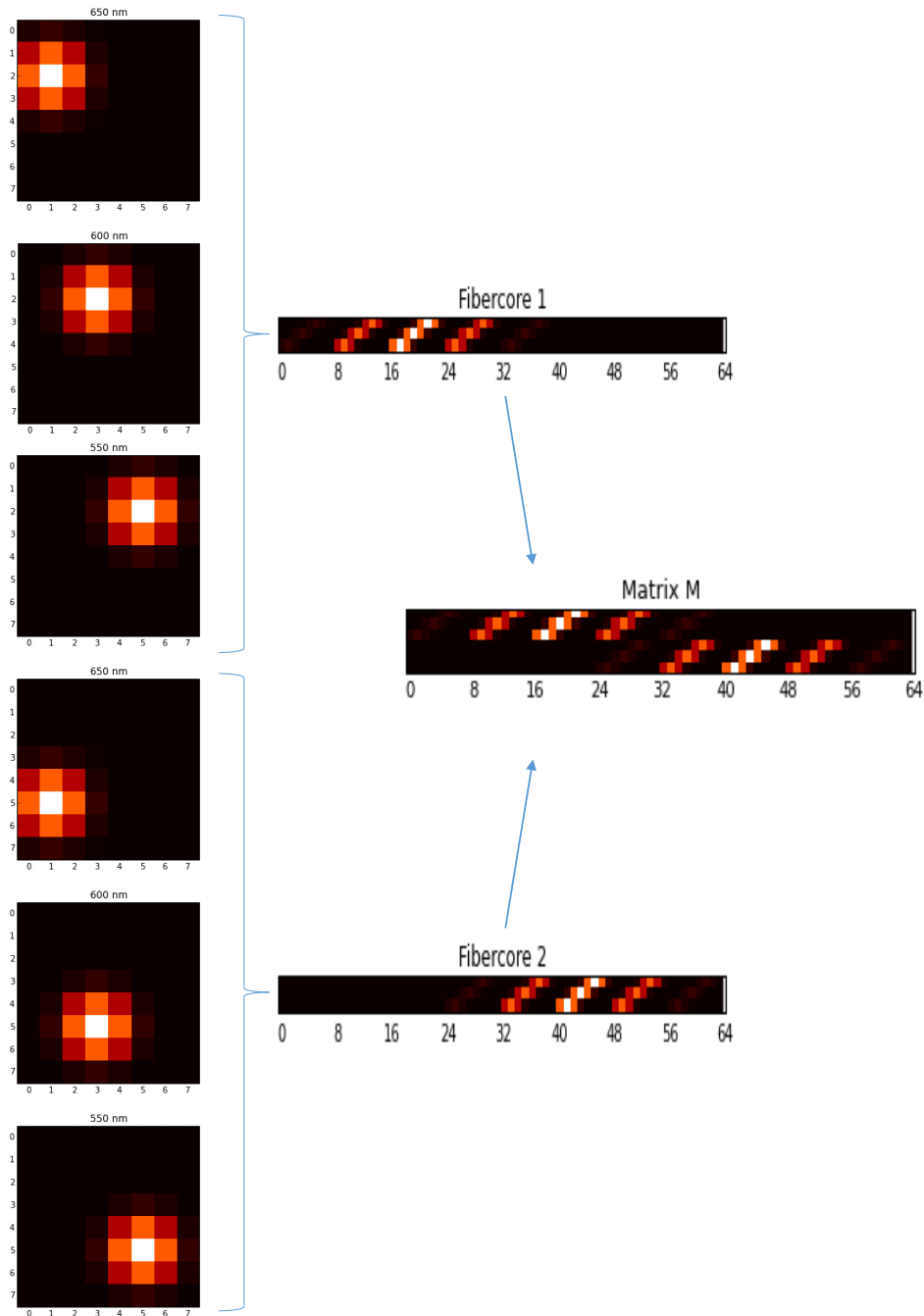
Figure 3.9: *A schematic explanation of the creation of the matrix* **M**, *containing two fibercores dispersed over three spectral bins. The Gaussians are first unraveled and then added.*

pact when inverted.

To eventually retrieve the amplitude profile, equation 3.16 is used.

$$\mathbf{f} = (\mathbf{M}^+)^* \mathbf{p} \tag{3.16}$$

There are two main factors which have to be optimized. First is r_{cond}, which determines the weight of the regularisation. Second is how far the Gaussians will be put apart in the matrix $\mathbf{M}$. The second is important because if the Gaussians overlap with one another, the resulting amplitude profile doesn't correspond with the actual intensity in that wavelength. But if the Gaussians are put apart too much, some information will not be used.

3.4   Testing of integrated set-up

After the spectrograph has been tested and its properties verified, the same will be done for the whole instrument. First, laserlight will go through an AO-system (in this thesis LEXI is used[33]). After which it will go through an APP which should null all fibercores surrounding one on which is focussed. After the APP, the light goes through the fibercores and the spectrograph.

By measuring the PSF before it enters the fiber and afterwards, the null can be measured. The light doesn't couple as well to some fibercores as to others, for which a correction has to be done based on the uniformly illuminated data.

4 | Results

4.1 Laser focus

The set-up has been aligned using a 633 nm laser uniformly over all fiber-cores. This results in the raw image as seen in figure 4.2. When looking at the images, one can observe that several fibercores are missing. The average FWHM detected is $58 \pm 8\mu m$ which corresponds with a MFD of $99 \pm 14\mu m$. Which is more than double than the expected $46\mu m$. However, the average distance between the fibercores in the image is $259 \pm 21\mu m$ which was expected ($10.53 * 25 = 263$).

## 4.2 Gaussian fitting of the Spectrum

In figure 4.2 an image of the spectrum is displayed on the left, on the right a fit is added of the tracks of the spectrum. Notice the overlap between the fibercores at the end (respectively beginning) and the crosstalk between them. The ideal rotation angle as described above has proven to be impossible, due to the crosstalk. The closest rotating angle was about ~17,5 degrees. This is almost double the calculated angle, which explains the overlap of the fibercores (the filters were designed for a longer spectrum).

As was described in the methods, the next important step was to fit the spectra. The fit is done using the linear least squares method. This was needed since the PeakUtils method fitted only a single Gaussian in each slice, which was insufficient to deal with the crosstalk as can be seen in 4.3. When the spectra are clearly distinguishable, all methods work equally well (4.3a). However, when the crosstalk becomes significant the interpolated single Gaussian fit quickly degenerates.

The least squares fitting takes more than 10 times as long as the PeakUtils method, but when the spectra tracks are finally fitted they should remain stable while only the amplitude changes.

4.3 Spectrum retrieval

After the spectra tracks have been located and the FWHM is retrieved from the laser image, the matrix needed for the linear algebraic extraction can
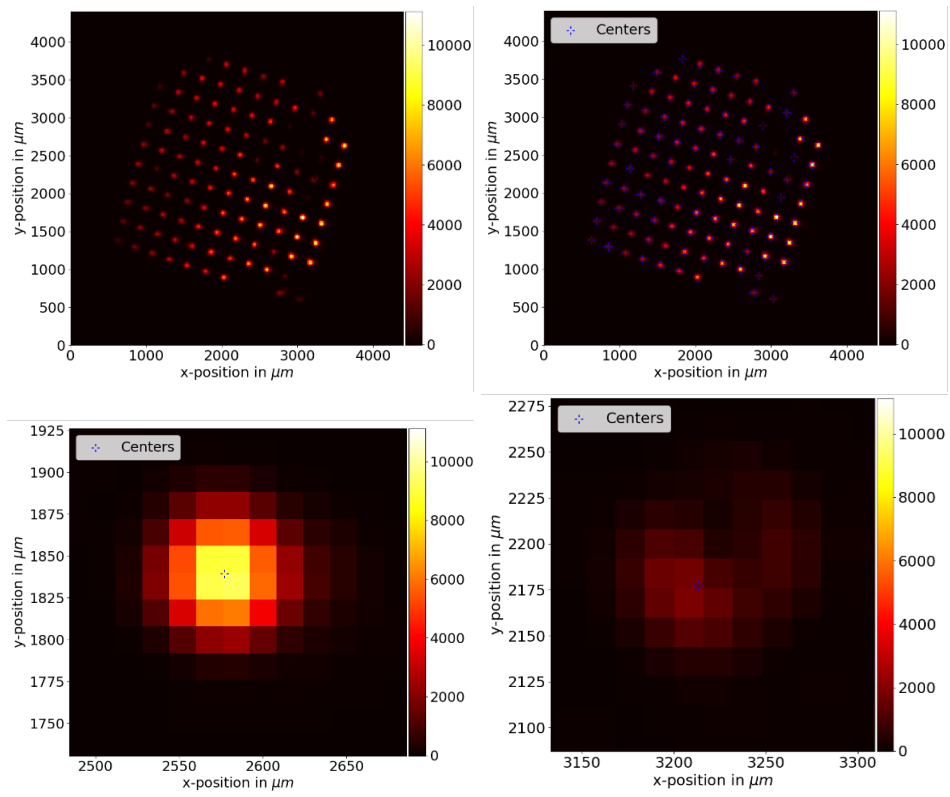
Figure 4.1: *An intensity-image after all elements have been focussed. The crosshairs in the top-right image depict where the centers are fitted on a sub-pixel level. The two images below depict two different spots, to show how well the centers can be found. The intensity is given in A.D.U.*
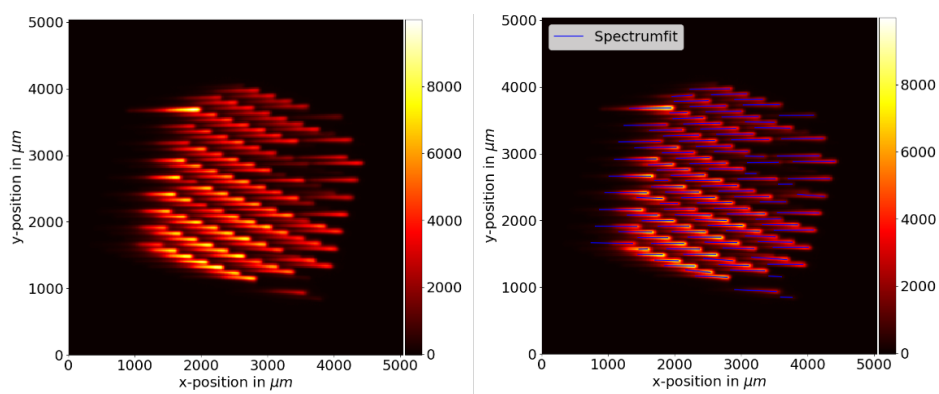
Figure 4.2: *The spectrum images. In the right image the fitted tracks of the spectra is displayed. Some couldn't be fitted due to too much overlap and some are cut-off because it began to fit different parts of the image*
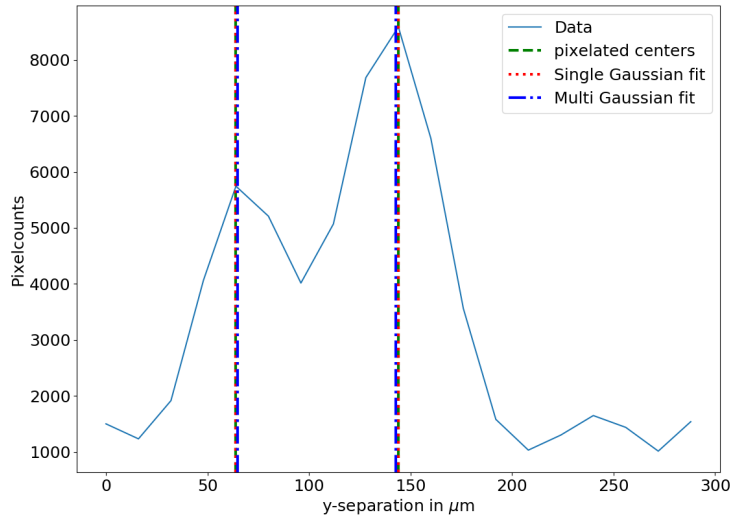
(a) *Two distinguishable Gaussians*
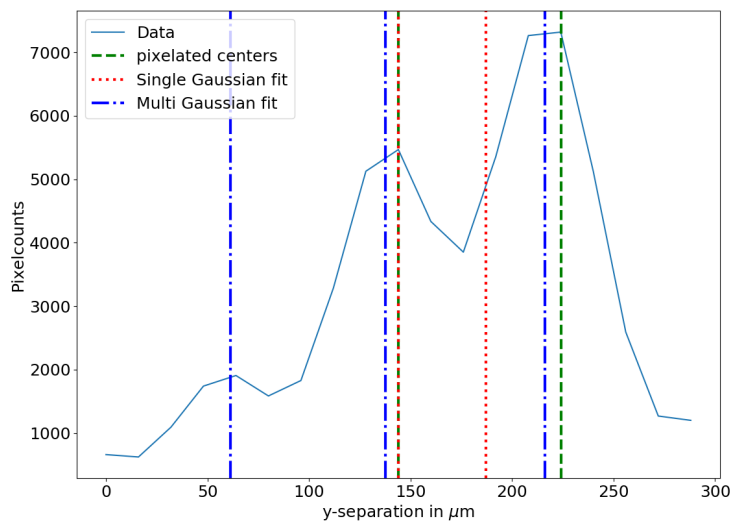
(b) *Three Gaussians, one of which is faint*

Figure 4.3: *Two different cross-sections in the y-direction of the spectra. The green dashed line is a single Gaussian fit without interpolation. The red dotted line is a single Gaussian fit with interpolation and the blue line dash-dotted line is a Multi-Gaussian fit using linear least squares.*
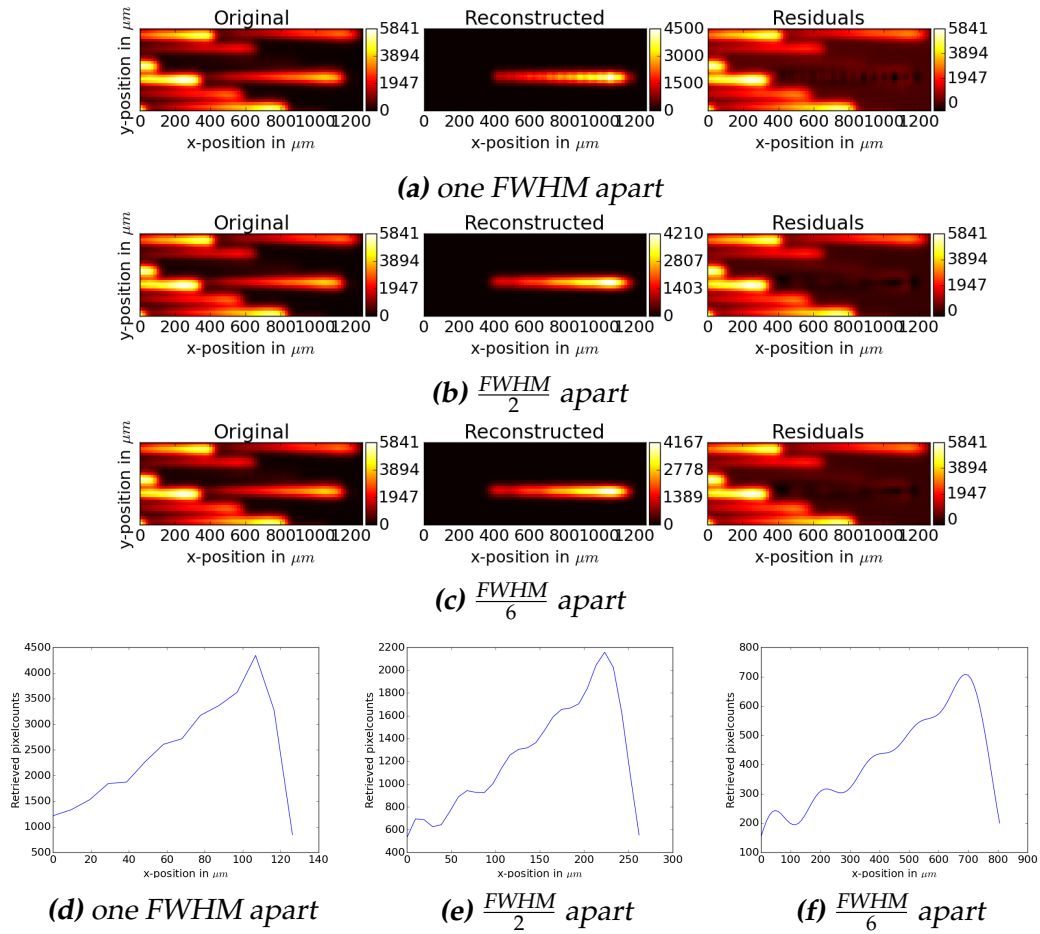
be created and inverted. If we subtract the reconstructed image from the original data and analyze the residuals we see that the residuals squared fall off asymptotically with the condition parameter. However, when the fitted tracks do not follow the spectra perfectly, a too low condition parameter induces a sinusoidal pattern in the retrieved amplitude profile.

Furthermore, there is the question of the spacing between the Gaussians. When they are fitted one FWHM next to each other, the reconstructed image becomes pixelated and the parts in between are not fitted as well as the parts where the Gaussian centers are. However, when the Gaussians are put closer together they will overlap and the retrieved amplitude profile reduces. For instance, see figure 4.4, when the Gaussians are separated one FWHM, there is a systematic overfitting (negative values regularly spaced), but when they are half a FWHM apart, the amplitude halves.

4.4   Integrating with LEXI

The creation of the clean PSF with the APP and the LEXI-instrument went quite well. However, when this was focussed on the fiber some problems arose. In the first run, we were not able to retrieve a clean PSF out of the fiber although the coupling seemed to be correct. Due to this, there was no way to measure the nulling of the system.

This nulling would have been another big challenge since the microlens array had been designed to couple with the output from the APP under a specific rotation. This rotation influenced the coupling tremendously, because it had to be correct within a tenth of a degree for the outer microlenses and within a degree for the inner lenslets. Since the orientation of the lenslets was not yet measurable, it was not possible to get this rotation correct.

(a) *one FWHM apart*

(b) $\frac{FWHM}{2}$ *apart*

(c) $\frac{FWHM}{6}$ *apart*

(d) *one FWHM apart*   **(e)** $\frac{FWHM}{2}$ *apart*   **(f)** $\frac{FWHM}{6}$ *apart*

Figure 4.4: *Three fits of the same spectra with each a different spacing between adjacent Gaussians in the matrix. The lineplots depict the amplitude profile, the images are from left to right the original image, the reconstructed spectrum and the resulting residuals.*
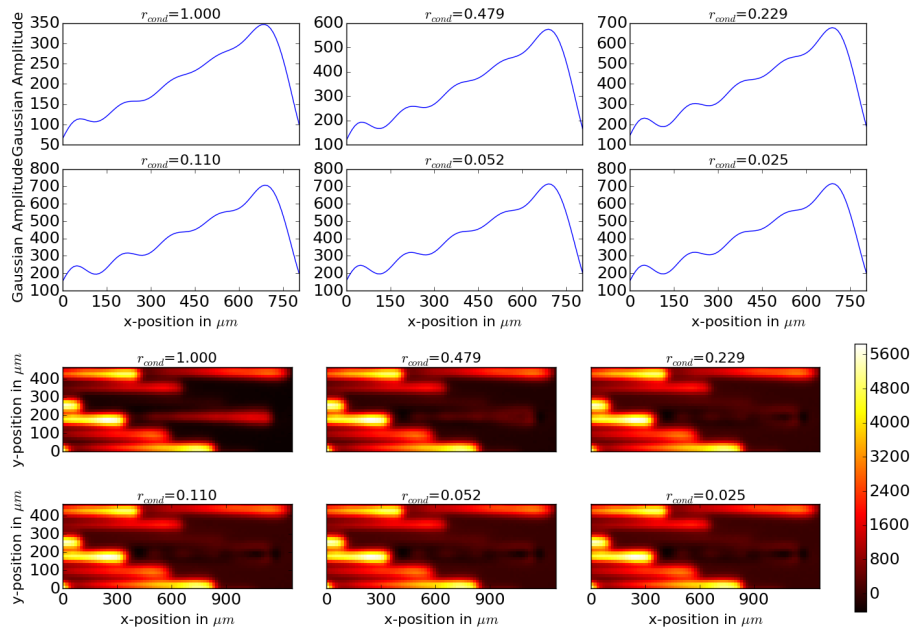
Figure 4.5: *The amplitude profile and residuals of one spectrum, after being fitted with 6 Gaussians per FWHM with different regularisation values. The colorbar depicts A.D.U.*
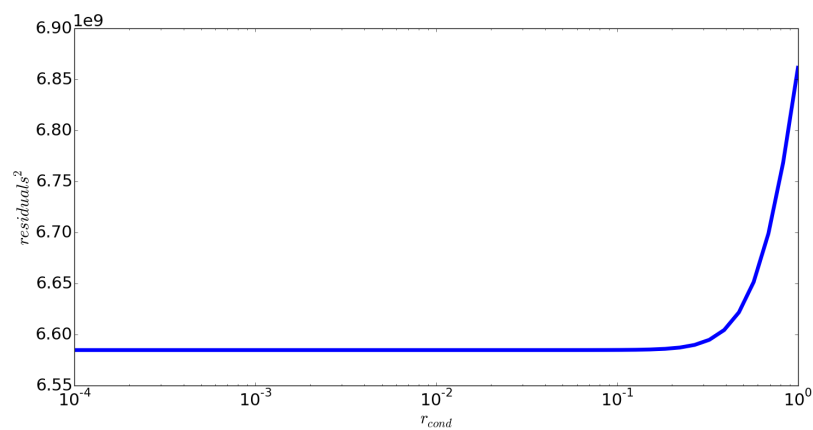
Figure 4.6: *A sum of all residuals squared after a fit with 6 Gaussians per FWHM*

5 | Discussion and Conclusion

5.1 set-up

After the alignment was completed, the first thing that caught the eye was the absence of some fibercores. This is believed to have two causes. First and foremost it could be the result of internal stresses and forces. Secondary to the primary reason, some imperfections could come from damages in mounting the bare fiber.

The fiber itself is big and complexly structured. This means that the polymers are under a lot of stress and experience much tension. When the microlenses are printed onto the fiber they will be affected by this as well. When the lenslets are put directly next to each other the stress from the fiber can influence the lenses and deform the array. The result of this is clearly visible in figure 5.1. When the microlenses are directly attached to each other, the resulting image is distorted and partly out of focus. But when they are attached indirectly with a sort of grid the image is much more clear. This second printed-upon fiber will be used for future measurements, because of its superiority.

The second cause for the varying intensity could be damages to the fiber. The fiber had to be carefully placed in a bare fibermount, whose working procedure demands the fiber to be cleaved afterwards to remove all damages done to the tip during mounting. According to the researcher who had printed the microlens array and the researchers who had created the fiber, this cleaving was extremely hard to do without the right tools and in-house knowledge. Thus we refrained from this cleaving, leaving the tip imperfect.

The second unexpected result was the factor two difference between the expected and the measured FWHM of the Gaussians and the spectra. This is believed to be mainly due to three factors: Residual aberrations, a too aggressive design and a difference in NA from the fiber. The first explanation would be a mistake in the magnification due to wrong positioning of the lenses, or a flaw in the design thereof. However, when we examined the gridspacing the magnification seemed to be as expected. A possible explanation could be that the focus was still off somehow, since

41
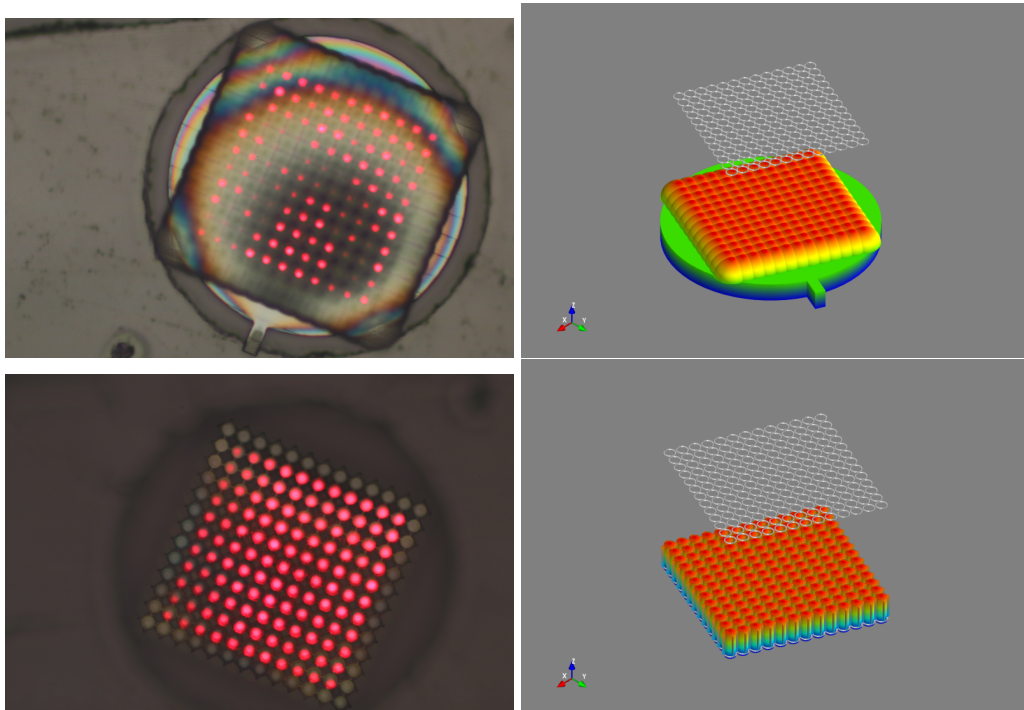
Figure 5.1: *On the left is the output of the laser after the fiber with the microlenses printed upon it as displayed on the right image. There is a much more uniform and in-focus image when the lenslets are separated instead of attached.*

there still seemed to be some residual aberrations such as astigmatism. The alignment of the microscope objective in combination with the fiber could have induced these kinds of aberrations easily.

Furthermore, there is the aggressiveness with which the spectrograph was designed. The design was made with the assumption that when the fibercores are spaced one MFD, they can be distinguished and measured. In practice this proved to be difficult; since there was a slight irregularity in the spacing of the fibercores, a MFD-separation for most two cores meant an overlap for some other two, which would mean an immediate loss of half the information.

Finally, the images in figure 5.1 suggest that the outgoing NA and MFD are not the same over the whole array and not what we expected. If this difference is too big, the microscope objective can fall short in its NA, disabling it to create a correct focus.

It is to be expected that a big improvement will be seen if the fiber is changed with the second fiber and the whole set-up is correctly re-aligned.

5.2   Extraction

The extraction seems to go relatively well, but there are still some hurdles to overcome. Although the position determination, creation of the matrix **M** and inversion go slow, it only has to be done once. After this, the only operation to retrieve the new amplitude profile is a matrix multiplication with the new data. However, the process of finding the spectra tracks can still be speeded up, as well as improved. The linear least-squares fit still wanders off the track sometimes to a brighter spectrum or is stopped prematurely due to a misfit. By inducing some extra constraints this process might be improved, while accessing more spectral information at the same time. In creating the matrix, one could also make use of known information such as relative intensities of the fibercores and the FWHM.

5.3   Integration with LEXI

Although the first trial set-up did not couple effectively, there is still a lot of room for improvement. When the correct orientation is found, we expect

to see a lot more and hopefully retrieve more information on the effective nulling of the system.

5.4   Future application: Active Speckle nulling

Speckles are the deformations of the linear wavefront as created from the star. There are two kinds of speckles: The first kind is created in the atmosphere by refraction and other effects such as scattering. These will be mostly nulled by the Adaptive Optic system (AO system), but this is not a perfect correction. The second originates from misalignments, unstable conditions and other errors in the optical system after the AO system. These are called non-common path errors or ghosts. Speckles represent the main problem with observing with earth-telescopes. To be able to produce science, one has to exert some form of speckle nulling (the removal of these atmospheric residues and non-common path errors). This is usually done with the use of a Deformable Mirror in an AO system [34] and post-processing of the data.

An useful characteristic of speckles for further research is their wavelength dependence. The atmosphere and optical system deform different wavelengths in different ways, thus the nulling could be very successful in one wavelength range, but have flaws in another. By making use of the spectrograph, we can measure these dependencies and adjust accordingly. Thus creating an active speckle control loop with the science data and the DM.

5.5   Next steps

For the spectrograph, the next important step would be to get a wavelength solution using multiple Lasers or an atomic line-lamp. Then a conversion of A.D.U. to actual photon count would be desirable. When the spectrograph has been successfully calibrated, a full integration with LEXI would be next. If the effective nulling of the set-up is measured, a definite proof of concept is finalised. If these measurements shows a significant improvement in the null, the first on-sky test can be done.

Bibliography

[1] M. Mayor and D. Queloz, *A jupiter-mass companion to a solar-type star*, Nature **378**, 355 (1995).

[2] J. Schneider, C. Dedieu, P. Le Sidaner, R. Savalle, and I. Zolotukhin, *Defining and cataloging exoplanets: the exoplanet.eu database*, Astronomy & Astrophysics **532**, A79 (2011).

[3] C. Lovis, I. Snellen, D. Mouillet, F. Pepe, F. Wildi, N. Astudillo-Defru, J. L. Beuzit, X. Bonfils, A. Cheetham, U. Conod, X. Delfosse, D. Ehrenreich, P. Figueira, T. Forveille, J. H. C. Martins, S. P. Quanz, N. C. Santos, H. M. Schmid, D. Ségransan, and S. Udry, *Atmospheric characterization of Proxima b by coupling the Sphere high-contrast imager to the Espresso spectrograph*, A&A **599** (2016).

[4] D. Mawet et al., *Review of small-angle coronagraphic techniques in the wake of ground-based second-generation adaptive optics systems*, SPIE (2012).

[5] I. A. Snellen, R. J. De Kok, E. J. De Mooij, and S. Albrecht, *The orbital motion, absolute mass and high-altitude winds of exoplanet HD 209458b*, Nature **465**, 1049 (2010).

[6] D. Mawet, G. Ruane, W. Xuan, D. Echeverri, N. Klimovich, M. Randolph, J. Fucik, J. K. Wallace, J. Wang, G. Vasisht, R. Dekany, B. Mennesson, E. Choquet, J.-R. Delorme, and E. Serabyn, *Observing Exoplanets with High-dispersion Coronagraphy. II. Demonstration of an Active Single-mode Fiber Injection Unit*, The Astrophysical Journal **838**, 92 (2017).

[7] E. H. Por, C. U. Keller, M. A. Kenworthy, D. S. Doelman, F. Snik, and M. J. Escuti, *The Single-mode Complex Amplitude Refinement (SCAR) coronagraph II . Lab verification , and towards the characterization of Proxima b*, page 1 (2017).

[8] M. Kenworthy, *http://home.strw.leidenuniv.nl/˜kenworthy/app*, 2017.

[9] D. Rouan, P. Riaud, A. Boccaletti, Y. Clénet, and A. Labeyrie, *The four quadrant phase mask coronagraph. I. Principle*, Pasp **112**, 1479 (2000).

[10] J. L. Codona, M. A. Kenworthy, P. M. Hinz, J. R. P. Angel, and N. J. Woolf, *A high-contrast coronagraph for the MMT using phase apodization:*

design and observations at 5 microns and 2 λ/D radius, in *SPIE Proceedings*, 2006.

[11] F. Snik, G. Otten, M. Kenworthy, M. Miskiewicz, M. Escuti, C. Packham, and J. Codona, *The vector-APP: a broadband apodizing phase plate that yields complementary PSFs*, in *SPIE Proceedings*, edited by R. Navarro, C. R. Cunningham, and E. Prieto, volume 8450, page 84500M, International Society for Optics and Photonics, 2012.

[12] G. P. P. L. Otten, F. Snik, M. A. Kenworthy, C. U. Keller, J. R. Males, K. M. Morzinski, L. M. Close, J. L. Codona, P. M. Hinz, K. J. Hornburg, L. L. Brickson, and M. J. Escuti, *On-sky performance analysis of the vector Apodizing Phase Plate coronagraph on MagAO/Clio2*, The Astrophysical Journal **834**, 175 (2017).

[13] S. Pancharatnam, *GENERALIZED THEORY OF INTERFERENCE*, Resonance, Journal of science **18**, 77 (2013).

[14] W. D. Heacox and P. Connes, *Optical fibers in astronomical instruments*, The Astronomy and Astrophysics Review **3**, 169 (1992).

[15] E. Hecht, *Optics*, Addison-Wesley, 3 edition, 1998.

[16] D. Bradbury, *https://sector.ca/the-internets-biggest-threat-lies-under-the-sea/*, 2018.

[17] K. Fidanboylu and H. Efendioglu, *Fiber optic sensors and their applications*, Proceedings of 5th . . . , 199 (2009).

[18] J. Verdeyen, *Laser electronics*, Prentice Hall, 1995.

[19] J. C. Knight, T. A. Birks, P. S. J. Russell, and D. M. Atkin, *All-silica single-mode optical fiber with photonic crystal cladding*, Optics Letters **21**, 1547 (1996).

[20] E. H. Por and S. Haffert, *The Single-mode Complex Amplitude Refinement (SCAR) coronagraph*, **7**, 1 (2017).

[21] J. A. Castro-almazán, B. G. Lorenzo, and M.-T. C, *Coherence time and turbulence velocity at the Roque de los Muchachos Observatory from G-SCIDAR*, (2017).

[22] G. H. Rieke, *Spectroscopy*, in *Measuring the Universe*, chapter Spectrosco, pages 154–188, Cambridge University Press, Cambridge, 2012.

[23] U. Mayor, M.; Pepe, F.; Queloz, D.; Bouchy, F.; Rupprecht, G.; Lo Curto, G.; Avila, G.; Benz, W.; Bertaux, J.-L.; Bonfils, X.; Dall, Th.; Dekker, H.; Delabre, B.; Eckert, W.; Fleury, M.; Gilliotte, A.; Gojak, D.; Guzman, J. C.; Kohler, D.; Lizon, J.-L.; Long, C. PHASE, and U. Mayor, M.; Pepe, F.; Queloz, D.; Bouchy, F.; Rupprecht, G.; Lo Curto, G.; Avila, G.; Benz, W.; Bertaux, J.-L.; Bonfils, X.; Dall, Th.; Dekker, H.; Delabre, B.; Eckert, W.; Fleury, M.; Gilliotte, A.; Gojak, D.; Guzman, J. C.; Kohler, D.; Lizon, J.-L.; Long, *Setting new standards with HARPS*, The Messenger **114**, 20 (2003).

[24] H. K. Chandrasekharan, F. Izdebski, I. Gris-Sánchez, N. KrstajiÄ, R. Walker, H. L. Bridle, P. A. Dalgarno, W. N. MacPherson, R. K. Henderson, T. A. Birks, and R. R. Thomson, *Multiplexed single-mode wavelength-to-time mapping of multimode light*, Nature Communications **8**, 1 (2017).

[25] S. Maruo, O. Nakamura, and S. Kawata, *Three-dimensional microfabrication with two-photon-absorbed photopolymerization*, Optics Letters **22**, 132 (1997).

[26] P.-I. Dietrich, M. Blaicher, I. Reuter, M. Billah, T. Hoose, A. Hofmann, C. Caer, R. Dangel, B. Offrein, U. Troppenz, M. Moehrle, W. Freude, and C. Koos, *In situ 3D nanoprinting of free-form coupling elements for hybrid photonic integration*, Nature Photonics **12**, 241 (2018).

[27] Shott, *Shott's optical glass datasheets*, Technical report, Shott North America, Inc., 2017.

[28] Edmund Optics Inc., *https://www.edmundoptics.com/document/download/359502*, 2018.

[29] Edmund Optics Inc., *https://www.edmundoptics.com/document/download/359531*, 2018.

[30] K. Horne, *An optimal extraction algorithm for CCD spectroscopy*, Publications of the Astronomical Society of the Pacific **98**, 609 (1986).

[31] A. S. Bolton and D. J. Schlegel, *Spectro-Perfectionism: An Algorithmic Framework for Photon Noise-Limited Extraction of Optical Fiber Spectroscopy*, Publications of the Astronomical Society of the Pacific , 100119133735095 (2009).

[32] D. C. Lay, S. R. Lay, and J. J. McDonald, *Linear Algebra and Its Applications*, Pearson Education, Inc., 5 edition, 2016.

[33] S. Y. Haffert, M. J. Wilby, C. U. Keller, and I. A. G. Snellen, *The Leiden EXoplanet Instrument (LEXI): a high-contrast high-dispersion spectrograph*, volume 9908, page 990867, International Society for Optics and Photonics, 2016.

[34] R. Tyson, *Principles Of Adaptive Optics.*, Elsevier Science, 1991.